

# Visualizing probabilistic models: Intensive Principal Component Analysis

Katherine N. Quinn, Colin B. Clement, Francesco De Bernardis, Michael D. Niemack, James P. Sethna<sup>1</sup>

<sup>1</sup>*Physics Department, Cornell University, Ithaca, NY 14853-2501, United States*

Unsupervised learning makes manifest the underlying structure of data without curated training and specific problem definitions. However, the inference of relationships between data points is frustrated by the ‘curse of dimensionality’ in high-dimensions. Inspired by replica theory from statistical mechanics, we consider replicas of the system to tune the dimensionality and take the limit as the number of replicas goes to zero. The result is the intensive embedding, which is not only isometric (preserving local distances) but allows global structure to be more transparently visualized. We develop the Intensive Principal Component Analysis (InPCA) and demonstrate clear improvements in visualizations of the Ising model of magnetic spins, a neural network, and the dark energy cold dark matter ( $\Lambda$ CDM) model as applied to the Cosmic Microwave Background.

Visualizing high-dimensional data is a cornerstone of machine learning, modeling, big data, and data mining. These fields require learning faithful and interpretable low-dimensional representations of high-dimensional data, and, almost as critically, producing visualizations which allow interpretation and evaluation of what was learned [1–4]. Unsupervised learning, which infers features from data without manually curated data or specific problem definitions [5], is especially important for high-dimensional, big data applications in which specific models are unknown or impractical. For high dimensions, the relative distances between features become small and most points are orthogonal to one another [6]. A trade-off between preserving local and global structure must often be made when inferring a low-dimensional representation.

Classic manifold learning techniques include linear methods such as Principal Component Analysis (PCA) [7] and multidimensional scaling (MDS) [8], which preserve global structure but at the cost of hiding local features. Existing nonlinear manifold learning techniques, such as t-distributed Stochastic Network Embedding (t-SNE) [9] and diffusion maps [10], preserve the local structure while only maintaining some qualitative global patterns such as large clusters. The Uniform Manifold Approximation (UMAP) [11] better preserves topological structures in data, a global property.

In this manuscript, we develop a new nonlinear manifold learning technique which achieves a compromise between preserving local and global structure. We accomplish this by developing an isometric embedding for general probabilistic models based on the replica trick [12]. Taking the number of replicas to zero, we reveal an *intensive* property – an information density characterizing the distinguishability of distributions – ameliorating the canonical orthogonality problem and ‘curse of dimensionality.’ We then describe a simple, deterministic algorithm that can be used for any such model, which we call Intensive Principal Component Analysis (InPCA). Our method quantitatively captures global structure while preserving local distances. We apply our visualization technique to the Ising model of magnetism in statistical physics, a convolutional neural network, and to the

dark energy cold dark matter ( $\Lambda$ CDM) model as applied to the Cosmic Microwave Background (CMB), revealing important features for all three.

## MODEL MANIFOLDS OF PROBABILISTIC MODELS

Any measurement obtained from an experiment with experimental uncertainty can be more generally seen as a probability distributions. For example, when some data  $x$  is observed with normally distributed noise  $\xi$  of variance  $\sigma^2$ , under experimental conditions  $\theta_j$ , a model is expressed as

$$x = f(\theta_j) + \xi \quad \text{where} \quad P(\xi) \sim \mathcal{N}(0, \sigma^2), \quad (1)$$

and  $f(\theta_i)$  is a prediction given the experimental conditions. This relationship is equivalent to saying that the probability of measuring data  $x$  given some conditions  $\theta$  is

$$P(x|\theta) \sim \mathcal{N}(f(\theta), \sigma^2). \quad (2)$$

Importantly, more complicated data (such as measurements with asymmetric uncertainties) can be generalized to non-Gaussian probability distributions (which incorporate skew, etc.). Measurements without an underlying model can also be seen as distributions, where a measurement  $x_i$  with uncertainty  $\sigma$  can be generalized to some distribution  $\mathcal{L}(x|x_i, \sigma)$ .

In general, a probabilistic model is defined by  $\mathcal{L}(x|\theta)$ , the likelihood of observing data  $x$  given parameters  $\theta = (\theta^1, \theta^2, \dots, \theta^m)$ . The *model manifold* is defined as the set of all possible predictions,  $\{\mathcal{L}(x|\theta_i)\}$ , which is a surface parameterized by the model parameters  $\{\theta_i\}$ . The parameter directions related to the longest distances along the model manifold have been shown to predict emergent behavior (how microscopic parameters come together, leading to macroscopic behavior) [13]. The boundaries of the model manifold represent simplified models which retain predictive power [14], and the constraint of data lying near the model manifold has been used to optimize experimental design [15]. We consider the following examples for studying the properties of

the intensive embedding and Intensive Principal Component Analysis: the first two—the Ising model and a neural network trained to recognize handwritten digits—are canonical examples, and the third is an important model for cosmology.

### HYPERSPHERE EMBEDDING

For data in high dimensions, almost all features are orthogonal to each other, and most proposed distance functions lose their ability to discriminate between the smallest and largest distances [16]. For probabilistic data this problem leads to most distributions having no overlap (dot product of zero). We can see this explicitly, if we consider:

$$\{z_{\mathbf{x}}(\boldsymbol{\theta}_i)\} = \left\{2\sqrt{\mathcal{L}(\mathbf{x}|\boldsymbol{\theta}_i)}\right\}. \quad (3)$$

This set lies on the positive orthant of an  $n$ -sphere of radius two, since all distributions are normalized and positive. The natural distance between points is the Euclidean distance,

$$\begin{aligned} d^2(\boldsymbol{\theta}_1, \boldsymbol{\theta}_2) &= \|\mathbf{z}(\boldsymbol{\theta}_1) - \mathbf{z}(\boldsymbol{\theta}_2)\|^2 \\ &= 8 \left(1 - \sqrt{\mathcal{L}(\mathbf{x}|\boldsymbol{\theta}_1)} \cdot \sqrt{\mathcal{L}(\mathbf{x}|\boldsymbol{\theta}_2)}\right)^2, \end{aligned} \quad (4)$$

where  $\cdot$  represents the inner product over  $x$ . As the dimensionality of  $x$  increases, the inner product in Eq. 4 becomes smaller as the probability is distributed over more dimensions: any small change in parameters has a compounding effect in high-dimensions, making the resulting distributions trivially distinguishable. Geometrically, all pairs of points become orthogonal, a distance  $\sqrt{8}$  apart, frustrating effective dimensional reductions and visualization.

To illustrate the problem with the hypersphere embedding, we consider a finite two-dimensional Ising Model. The Ising Model of magnetism predicts the likelihood of observing a particular spin configuration on a lattice [13]. Holding temperature fixed at one, we vary external magnetic field (from -1.3 to 1.3), and nearest neighbour coupling (from -0.4 to 0.6) exploring both the ferromagnetic and anti-ferromagnetic regime. We sampled this regime using a Monte Carlo method weighted by Jeffreys Prior, generating a set  $X_{ij} = \{\mathbf{z}_i(\boldsymbol{\theta}_j)\}$ . We visualize the model manifold in the  $n$ -sphere embedding of Eq. 3 by projecting the predictions onto the first three principal components of  $X$ . Figure 1(a) shows the model manifold of a  $2 \times 2$  Ising model which is embedded in  $2^4$  dimensions. Figure 1(b) shows a  $4 \times 4$  Ising model, of dimension  $2^{16}$ . As the dimension is increased from  $2^4$  to  $2^{16}$ , we see the points starting to wrap around the hypersphere, becoming equidistant and indistinguishable – an effect which can be duplicated by considering four replicas of the  $2 \times 2$  system, as shown in Fig. 1(c). This problem has been referred to as a loss of relative contrast or the concentration of distances, and has been found to plague almost

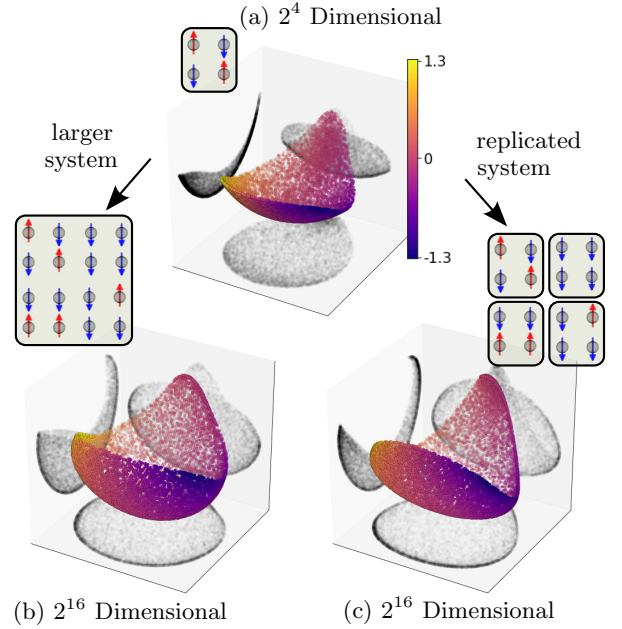


FIG. 1. **Hypersphere embedding**, illustrating an embedding of the two dimensional Ising model. Points were generated through a Monte Carlo sampling and visualized by projecting the probability predicts onto the first 3 principal components. The points are colored by magnetic field strength. As the system size increases from  $2 \times 2$  to  $4 \times 4$ , the orthogonality problem is demonstrated by an increase in ‘wrapping’ around the hypersphere. This effect can be also be produced by instead considering four replicas of the original system, motivating the replica trick which takes the embedding dimension or number of replicas to zero.

any conceivable distance measure in dimensions as low as ten [16].

The hypersphere embedding of Eq. 3 does not solve the high dimensional orthogonality problem, but it is *isometric*: it preserves local structure of the model manifold. More specifically, the Euclidean metric of this embedding is equal to the Fisher Information metric  $\mathcal{I}$  of the model manifold [17]:

$$d^2(z_i, z_i + dz_i) = \sum_i dz_i dz_i = \sum_{kl} \mathcal{I}_{kl} d\theta_k d\theta_l. \quad (5)$$

The Fisher Information Metric (FIM) is the natural metric of the model manifold and is an important quantity in inference and information geometry [18]. In the next section we leverage the replica trick to discover an embedding which is not only isometric but also ameliorates the high-dimensional wrapping around the  $n$ -sphere.

### REPLICA THEORY AND THE INTENSIVE EMBEDDING

We saw in Fig. 1 that increasing the dimension of the data led to a saturation of the distance function Eq. 4,

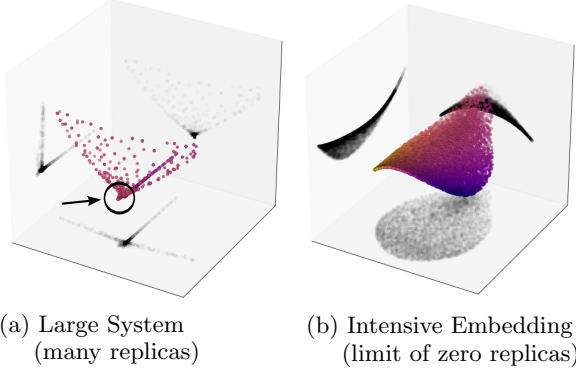


FIG. 2. **Replicated Ising Model** illustrating the derivation of our intensive embedding. All points are coloured by magnetic field strength, as in Fig. 1. (a) Large dimensions are characterized by large system sizes; here we mimic a  $128 \times 128$  Ising model which is of dimension  $2^{128^2}$ . The orthogonality problem becomes manifest as all points are effectively orthogonal, producing a useless visualization with all points clustered in the cusp. (b) Using replica theory, we tune the dimensionality of the system and consider the limit as the number of replicas goes to zero. In this way, we derive our intensive embedding. Note that the z-axis reflects a negative-squared distance, a property which allows violations of the triangle inequality and is discussed in the text.

and a concomitant loss of distinguishability between features. We also saw the same effect could be achieved by including copies or replicas in the data. Inspired by this observation we are going to seek an *intensive* embedding of the data, that is an embedding which does not scale with the dimensionality of the model predictions.

Taking the number of replicas to infinity rapidly hides useful information, as shown in Fig 2(a) where the points all cluster together, stymieing dimensionality reduction. Just as the energy of a system is extensive, growing with system size, and temperature is intensive, independent of system size, we want an intensive manifold embedding that reflects the information *density*. We achieve this by taking the limit of *zero* replicas, dividing our distance by the number of replicas to obtain a well-defined limit. Figure 2(b) shows the result of this analysis, the *Intensive Embedding*, where the distance concentration has been cured and the points on the model manifold are distinguishable.

To find the intensive embedding, we must first find the distance between replicated models. The likelihood for  $N$  replicas of a system is given by their product

$$\mathcal{L}(\{\mathbf{x}_1, \dots, \mathbf{x}_N\}|\boldsymbol{\theta})^{(N)} = \mathcal{L}(\mathbf{x}_1|\boldsymbol{\theta}) \cdots \mathcal{L}(\mathbf{x}_N|\boldsymbol{\theta}), \quad (6)$$

where the set  $\{\mathbf{x}_1, \dots, \mathbf{x}_N\}$  represents the observed data in the replicated systems. Writing the inner product or cosine angle between two distributions as

$$\langle \boldsymbol{\theta}_1; \boldsymbol{\theta}_2 \rangle = \sqrt{\mathcal{L}(\mathbf{x}|\boldsymbol{\theta}_1)} \cdot \sqrt{\mathcal{L}(\mathbf{x}|\boldsymbol{\theta}_2)}, \quad (7)$$

and using Eq. 4, we can calculate the distance per replica

$d_N^2$  between two points on the model manifold:

$$d_N^2(\boldsymbol{\theta}_1, \boldsymbol{\theta}_2) = \frac{d^2(\boldsymbol{\theta}_1, \boldsymbol{\theta}_2)}{N} = -8 \frac{\langle \boldsymbol{\theta}_1; \boldsymbol{\theta}_2 \rangle^N - 1}{N}. \quad (8)$$

We are now poised to define the *intensive* distance

$$d_I^2(\boldsymbol{\theta}_1, \boldsymbol{\theta}_2) = \lim_{N \rightarrow 0} d_N^2(\boldsymbol{\theta}_1, \boldsymbol{\theta}_2) = -8 \log \langle \boldsymbol{\theta}_1; \boldsymbol{\theta}_2 \rangle. \quad (9)$$

The last equality is achieved using the standard trick in replica theory,  $\lim_{N \rightarrow 0} x^N / N - 1/N = \log x$ , which has provided fruitful insights and correct solutions to challenging problems in statistical physics [19]. The trick is most evident using the identity  $x^N = \exp(\log Nx) \approx 1 + N \log x$ . Note that the intensive distance obtained here is related to the Hellinger distance and proportional to the Bhattacharyya distance [20], both of which are used to characterize distances between probability distributions.

One can check that the intensive distance is isometric:

$$d_I^2(\boldsymbol{\theta}, \boldsymbol{\theta} + \delta\boldsymbol{\theta}) = \delta\theta^\alpha \delta\theta^\beta g_{\alpha\beta} = \delta\theta^\alpha \delta\theta^\beta \mathcal{I}_{\alpha\beta}, \quad (10)$$

where again  $\mathcal{I}$  is the Fisher Information Metric in Eq. 5. Therefore the intensive embedding preserves local structure, but it also ameliorates the orthogonality problem: as dimensionality increases the distance between points can go to infinity, rather than to the finite radius of the hypersphere embedding. In this way, distances in the intensive embedding maintain distinguishability in high dimensions, as illustrated in Fig. 2(b).

### Connection to Least Squares

We can gain some intuition about the intensive embedding by considering the concrete and canonical paradigm of models with additive white Gaussian noise, usually called a nonlinear least-squares model. For some data  $x_i$  and a model  $f_i(\boldsymbol{\theta})$ , the likelihood  $\mathcal{L}(\mathbf{x}|\boldsymbol{\theta})$  is defined by

$$\log \mathcal{L}(\mathbf{x}|\boldsymbol{\theta}) = \sum_i \frac{(f_i(\boldsymbol{\theta}) - x_i)^2}{2\sigma_i^2} - \log \mathcal{Z}(\boldsymbol{\theta}), \quad (11)$$

where  $\mathcal{Z}$  sets the normalization. A straightforward evaluation of the intensive distance given by Eq. 9 finds for the case of nonlinear least squares that

$$d_I^2(\boldsymbol{\theta}_1, \boldsymbol{\theta}_2) = \sum_i \frac{(f_i(\boldsymbol{\theta}_1) - f_i(\boldsymbol{\theta}_2))^2}{\sigma_i^2}, \quad (12)$$

so that the intensive distance is simply the variance-scaled Euclidean distance between model predictions.

### INTENSIVE PRINCIPAL COMPONENT ANALYSIS

Classical Principal Component Analysis (PCA) takes a set of data examples and infers features which are uncorrelated. [7]. The steps are essentially: given a matrix of data examples  $X$ , find a basis using the SVD (or

equivalently, the basis of the covariance matrix of  $X$ ), and then projecting the mean-shifted rows of  $X$  onto this basis. If successful, the first few projections, which are by definition linearly uncorrelated, should be interpretable features of the data. Specifically for  $X \in \mathbb{R}^{m \times p}$ , a mean-shifted matrix  $M_{ij} = X_{ij} - \bar{X}_i = PX$  is computed, where  $P_{ij} = \delta_{ij} - 1/p$  is the mean-shift projection matrix and  $p$  is the number of sampled points. The covariance and its eigenvalue decomposition are computed

$$\text{cov}(X, X) = \frac{1}{p} M^T M = X^T P P X = V \Sigma V^T. \quad (13)$$

The orthogonal columns of the matrix  $V$  are the natural basis onto which the rows of  $M$  are projected:

$$MV = (UDV^T)V = UD = U\sqrt{\Sigma}, \quad (14)$$

where we have used the singular value decomposition of  $M$ . The principal components of the data  $X$  are given by  $U\sqrt{\Sigma}$ .

The components can also be obtained by performing an eigenvalue decomposition on the cross-covariance matrix,  $MM^T$ , since

$$MM^T = PXX^T P = (UDV^T)(UDV^T)^T = U\Sigma U^T \quad (15)$$

The eigenbasis of the cross-covariance is the natural basis for the components of the data, and the eigenbasis of the covariance is the natural basis of the data points. For us this flexibility is invaluable, as the cross-covariance is more natural for expressing the distances between distributions of different parameters. Writing our data matrix as  $X_{ij} = z_i(\theta_j)$  using Eq. 3, the cross-covariance for the unreplicated system is

$$(MM^T)_{ij} = (z(\theta_i) - \bar{z}) \cdot (z(\theta_j) - \bar{z}) = (PXX^T P)_{ij} \quad (16)$$

where  $\bar{z}$  is the average over all sampled parameters. Using the definition of  $z$  in Eq. 6, the replicated cross-covariance is

$$(MM^T)_{ij}^{(N)} = 4 \langle \theta_i; \theta_j \rangle^N + \frac{4}{p^2} \sum_{k,k'=1}^p \langle \theta_k; \theta_{k'} \rangle^N, \\ - \frac{4}{p} \sum_{k=1}^p \left( \langle \theta_i; \theta_k \rangle^N + \langle \theta_j; \theta_k \rangle^N \right) \quad (17)$$

where  $p$  is the number of sampled points. We can then take limit as the number of replicas goes to zero,

$$W_{ij} = \lim_{N \rightarrow 0} \frac{1}{N} (MM^T)_{ij}^{(N)}. \quad (18)$$

We can write out the replicated cross-covariance matrix explicitly as

$$W_{ij} = 4 \log \langle \theta_i; \theta_j \rangle + \frac{4}{p^2} \sum_{k,k'=1}^p \log \langle \theta_{k'}; \theta_k \rangle \\ - \frac{4}{p} \sum_{k=1}^p (\log \langle \theta_i; \theta_k \rangle + \log \langle \theta_j; \theta_k \rangle) \quad (19)$$

$$= (PLP)_{ij} \quad (20)$$

where  $L_{i,j} = 4 \log \langle \theta_i; \theta_j \rangle$  and  $P$  is the same projection matrix as defined above. In taking the limit of zero replicas, the structure of the cross-covariance has transformed

$$PXX^T P \xrightarrow{N \rightarrow 0} PLP, \quad (21)$$

and thus the symmetric Wishart structure is lost. It is therefore possible to obtain negative eigenvalues in this decomposition, which give rise to imaginary components in the projections. This effect is explored in greater detail in the following section.

In summary, Intensive Principal Component Analysis (InPCA) is defined by the following procedure:

1. *Generate a set of probability distributions,  $\{\mathcal{L}(\mathbf{x}|\theta_1), \dots, \mathcal{L}(\mathbf{x}|\theta_p)\}$ , or interpret some data as a set of distributions.*
2. *Compute the cross-covariance matrix:* Compute  $W_{ij}$  as derived in Eq. 19.
3. *Compute the eigenvalue decomposition  $W = U\Sigma U^T$ .*
4. *Compute the coordinate projections or intensive principal components  $T = U\sqrt{\Sigma}$ .*
5. *Plot the projections* using the columns of  $T$ . It is possible to generate as many projections as data points sampled in step 1.

In Fig. 3, we visualize the first three components of the model manifold for the three models considered in this manuscript. We visualize these models by using the Intensive Principal Component Analysis (InPCA) to extract low-dimensional representations.

### Ising Model

The Ising Model is shown in Fig. 3(a). The first two directions from InPCA correspond to the magnetic field strength and the coupling between neighboring spins. Visualizing the manifold with InPCA, we therefore extract four important regimes: ferromagnetic and anti-ferromagnetic, as well as spins in a large positive and large negative field.

### Convolution Neural Network

The second model we consider is a two layer convolution neural network, constructed using TensorFlow [21] and trained on the MNIST data set of hand-written digits [22]. A set of 55,000 images were used to train the network, which was then used to predict the likelihood that an additional set of 10,000 images are each classified as a specific digit between 0 and 9. We use softmax [23] to calculate the probabilities from the category estimates

supplied by the network. The InPCA projections of the neural network output in Fig. 3(b) show the clustering learned by the neural network.

### $\Lambda$ CDM Cosmological Model

The final model used in this manuscript is the dark energy cold dark matter ( $\Lambda$ CDM) cosmological model. This model predicts the angular power spectrum of temperature and polarization anisotropies in sky maps of the Cosmic Microwave Background (CMB). Observations of the CMB from telescopes on satellites, balloons, and the ground provide thousands of independent measurements from large angular scales to a few arcminutes, that are used to fit model parameters. The  $\Lambda$ CDM model we consider has six parameters, the Hubble constant ( $H_0$ ) which we sampled in a range of 20 to 100  $km\ s^{-1}\ Mpc^{-1}$ , the physical baryon density ( $\Omega_b h^2$ ) and the physical cold dark matter density ( $\Omega_c h^2$ ) both sampled from 0.0009 to 0.8, the primordial fluctuation amplitude ( $A_s$ ) sampled from  $10^{-11}$  to  $10^{-8}$ , the scalar spectral index ( $\eta$ ) sampled from 0 to 0.98, and the optical depth at reionization ( $\tau$ ) sampled from 0.001 to 0.9. We use the CAMB software package to generate power spectra [24], and perform a Monte Carlo sampling of 50,000 points around the best fit parameters provided by the 2015 Planck data release [25]. We weighted the sampling based on proximity to Planck data. In Fig. 3(c), we see that InPCA extracts two components corresponding to  $A_s$  and the Hubble constant, parameters which control the two most dominant features in Planck data.

### PROPERTIES OF THE INTENSIVE EMBEDDING AND INPCA

The new space characterized by our intensive embedding has two weird properties: first it is formally zero dimensional yet there are multiple orthogonal directions upon which it can be projected, and second it is Minkowski-like, in that it has negative squared distances, violating the triangle inequality. We posit that, fundamentally, this second property is what allows InPCA to cure the orthogonality problem.

We begin with a discussion of the the zero-dimensional nature of the embedding space. When performing standard PCA, the embedding space is characterized by the projection matrix. In the case of positive integer number of replicas it is a normalized linear combination of state vectors or probability functions. The dimension is proportional to the number of replicas, and so in the case of non-integer replicas the space becomes ‘fractional’ in dimension and in the limit of zero replicas ultimately goes to zero. However, it is still possible to obtain projections themselves along the dominant components of this space, by leveraging the cross-covariance instead of the

covariance, summarized in step 2 of our algorithm.

We now discuss the Minkowski-like nature of InPCA. In the limit of zero replicas is in Eq. 19, the positive-definite, Wishart structure of the cross-covariance matrix is lost, as shown in Eq. 21. Positive eigenvalues are no longer guaranteed, and thus it is possible to have negative squared distances, or, equivalently, purely imaginary projections. We conjecture that this allows the model manifold to be ‘unwound’ from the  $n$ -sphere. Consider, for example, a biased coin. In a useful embedding, one would wish ‘all-heads’ and ‘all-tails’ states to be infinitely far apart; the Hellinger distance in Eq. 4 is finite, but the intensive distance between these states is infinite. Figure 4 shows the top two InPCA components of the biased coin model manifold, which are related to the bias and variance of the coin. Curves of constant distance from a fair coin are hyperbolas (gray lines): two points can be finitely far from a fair coin but infinitely far from each other.[? ]

### Comparing with t-SNE and Diffusion Maps

We compare our manifold learning technique to two standard methods, t-SNE and the diffusion maps, applied to the model manifold of the  $\Lambda$ CDM model fitting the cosmic microwave background data (described in the first section). In order to apply t-SNE and the diffusion map to probabilistic data we must provide a distance. A common distance used to characterize probability distributions is given by the Kullback-Leibler divergence [26], however it is not symmetric and thus will not work with these methods. We therefore use our intensive distance, from Eq. 9, for consistency and ease of comparison.

In figure 5 we show the first three components of the manifold embedding for InPCA, t-SNE and diffusion maps. In all three cases, the first component from each method is directly related to the primordial fluctuation amplitude  $A_s$ , which reflects the amplitude of density fluctuations in the early universe, and is the dominant feature in real data [25]. The second InPCA component predicts the Hubble constant, whereas the diffusion map predicts the scalar spectral index (a reflection of the size variance of primordial density fluctuations).

An important difference between InPCA and other methods is that InPCA has no tunable parameters, and is a geometric object defined entirely by the model distribution. For example, t-SNE embeddings rely on parameters such as the perplexity, a learning rate, and a random seed (yielding non-deterministic results), and the diffusion maps rely on a diffusion parameter and choice of diffusion operator, all of which must be manually optimized to obtain good results.

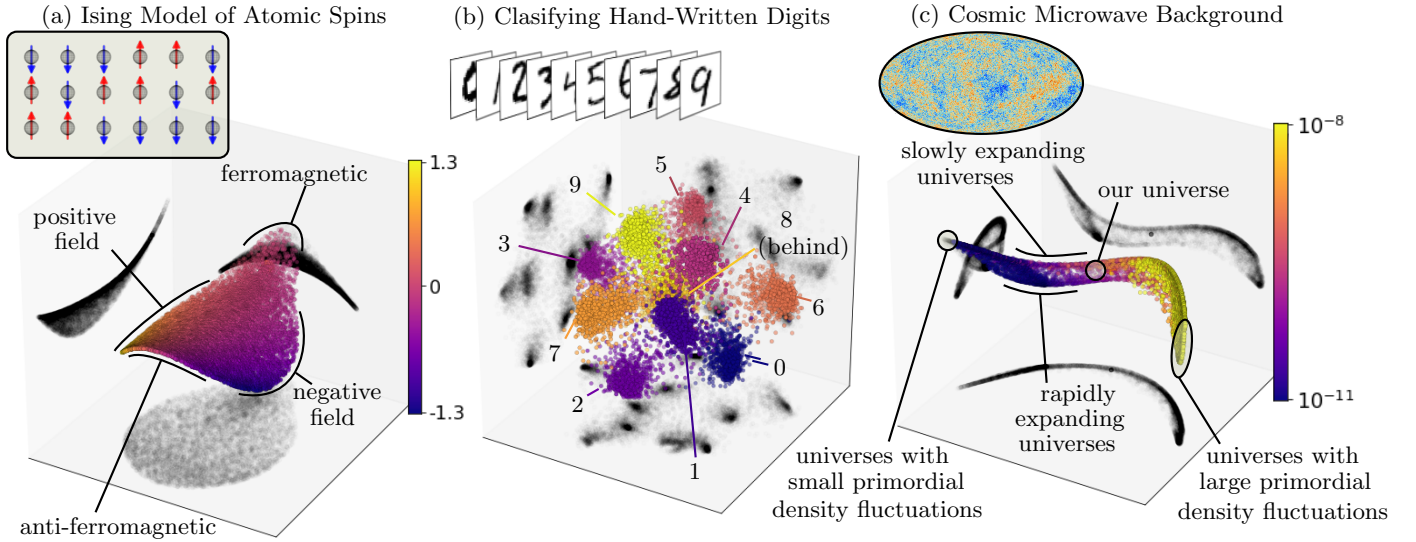


FIG. 3. **InPCA** of probabilistic models considered in this manuscript. (a) The Ising model of atomic spins, which predicts the likelihood of observing a particular spin configuration given a temperature, magnetic field, and spin couplings [13]. Large positive and negative magnetic fields (making all spins aligned up or down the most probable state), and ferromagnetic/anti-ferromagnetic regimes are located far apart from each other. Note that the z-axis of this plot reflects a negative-squared component, described in the text. (b) Visualization of predictions made by a convolutional neural network created with TensorFlow [21] on MNIST data [22]. The network was trained using 55,000 images, and then tested on an additional set of 10,000. Probabilities are generated by performing softmax [23] on the resulting estimates. Points are coloured by digit type, and the clustering of points is a reflection of how well the network ‘sees’ the test images. (c) The six parameter dark energy cold dark matter ( $\Lambda$ CDM) cosmological model predictions of temperature and polarization power spectra in the CMB. The model does not predict an exact sky map, such as the temperature sky map from the Planck 2015 data release [25] shown in the upper left, but *likelihood* of observing a particular sky map power spectrum. Here the model manifold is coloured by the primordial fluctuation amplitude, which characterizes the size of primordial density fluctuations in the early universe. The ‘height’ is determined by the Hubble constant, describing the rate of expansion. Note that the z-axis reflects a negative-squared distance, discussed in the text. For (a) and (c), rotating the model manifold to visualize on a plane should formally involve Lorentz transformations, omitted in this analysis for clarity.

## SUMMARY

In this manuscript, we introduce an unsupervised manifold learning technique, InPCA, which captures low-dimensional features of general, probabilistic models with wide-ranging applicability. We consider replicas of a probabilistic system to tune its dimensionality and consider the limit of zero replicas, deriving an *intensive* embedding that ameliorates the canonical orthogonality problem. Our intensive embedding provides a natural, meaningful way to characterize a symmetric distance between probabilistic data.

How can such an embedding space be useful? There are far ranging applications for manipulating and visualizing large dimensional data sets. In Fig. 3(c) we show the distinguishability within the six-parameter family of  $\Lambda$ CDM models given recent CMB measurements. InPCA generates an interesting hierarchy of parameter importance, and could be used to guide the design of future instruments to better measure cosmological parameters such as the neutrino mass sum, the number of relativistic species, and the tensor-to-scalar ratio. Figure 3(a) illustrates the family of behaviors exhibited by Ising models, and could be coarse-grained by sam-

pling a sub-grid of spins in a larger Ising model. The renormalization group tells us that this coarse-grained model can be rescaled to match the original model at renormalized parameters; distance in the intensive metric embedding could be a systematic, principled way of matching these parameters. Finally, an area of great impact is in machine learning, in particular visualizing predictions from trained neural networks, such as those shown in Fig. 3(b). These methods produce complex, high-dimensional probabilistic models, and InPCA can be used to deterministically visualize how well the neural network ‘sees’ the input images.

We thank Mark Transtrum for guidance on algorithms and for useful conversations. KNQ was supported by a fellowship from the Natural Sciences and Engineering Research Council of Canada (NSERC), and JPS and KNQ were supported by the National Science Foundation through grant NSF DMR-1312160 and DMR-1719490. MDN was supported by NSF grant AST-1454881.



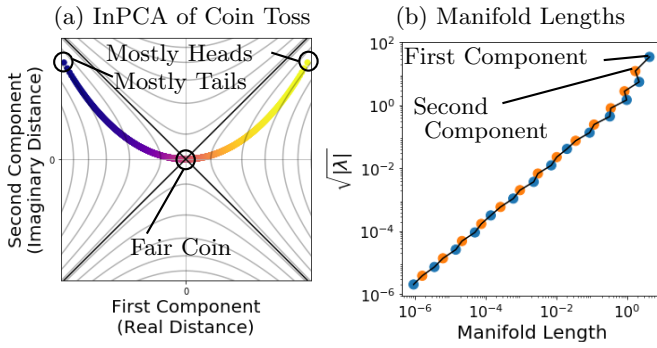


FIG. 4. **Biased coin toss** as visualized using InPCA. (a) A simple model of a biased coin is a one-dimensional object, since there is only one model parameter: the odds ratio of heads to tails, used to color the figure. Yellow has  $P(\text{Heads}) = 1$  and blue has  $P(\text{Tails}) = 1$ . The figure shows the embedding distances reflecting each coin's distance from a fair coin in the first two components from InPCA. Note that the first two components correspond to meaningful quantities, the coin bias and variance, yet the first is real while the second is imaginary. We can see how the ‘unwinding’ effect can take place through the negative-squared distances. Contour lines represent constant distances from a fair coin and are hyperbolas: points can be a finite distance from a fair coin yet an infinite distance from each other. In this way, as coins become increasingly biased their distance from each other can go to infinity (because an outcome of a coin which always lands heads will never be the same as an outcome of a coin which always land tails) yet all remain a finite distance from a fair coin. Note that all points are in the left and right portions of the figure, representing *net* positive distances (the intensive distances are all positive). (b) There are as many projections of the manifold as sampled points, however there is a hierarchy of importance given by the size of the different projections (shown here for the first 25 projections). The eigenvalues from the cross-covariance matrix (Eq. 19) for the coin toss alternate as real and imaginary (blue points are real values, orange are imaginary), and correspond to the manifold lengths. In this way, InPCA provides a quantitative measure of the global structure.

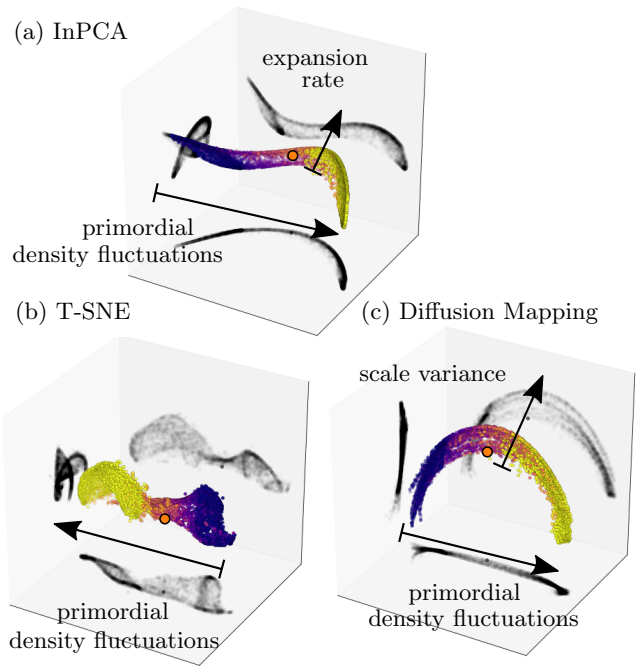


FIG. 5. **Model manifold of the six parameter dark energy cold dark matter ( $\Lambda$ CDM) cosmological model predictions of temperature and polarization power spectra in the CMB** using InPCA, t-SNE and the diffusion map. Here the model manifold is colored by the primordial fluctuation amplitude, the most prominent feature in CMB data. (a) InPCA extracts, as the first and second component, this amplitude term as well as the Hubble constant (reflected in the location of the first baryon acoustic oscillation in the CMB power spectrum). These parameters control the two most dominant features in the Planck data, and so reflect a physically meaningful hierarchy of importance. In contrast, (b) t-SNE only extract the amplitude term and (c) the diffusion map extract the amplitude term and a different parameter, the scalar spectral index  $\eta$ , which reflects the scale variance of the density fluctuations in the early universe. Note that InPCA is parameter free, whereas t-SNE and diffusion mapping required tuning of plotting parameters to optimize the visualization. In all plots, the orange point represents our universe as represented by Planck 2015 data.

- 
- [1] de Oliveira MCF, Levkowitz H (2003) From visual data exploration to visual data mining: a survey. *IEEE Transactions on Visualization and Computer Graphics* 9(3):378–394.
  - [2] Liu S, Maljovec D, Wang B, Bremer PT, Pascucci V (2017) Visualizing High-Dimensional Data: Advances in the Past Decade. *IEEE Transactions on Visualization and Computer Graphics* 23(3):1249–1268.
  - [3] Lee JA, Verleysen M (2007) *Nonlinear Dimensionality Reduction*. (Springer, NY).
  - [4] Zimek A, Schubert E, Kriegel HP (2012) A Survey on Unsupervised Outlier Detection in High-Dimensional Numerical Data. *Statistical Analysis and Data Mining* 5(5):363–387.
  - [5] Murphy KP (2012) *Machine Learning: A Probabilistic Perspective*. (The MIT Press).
  - [6] Kriegel HP, Kröger P, Zimek A (2009) Clustering high-dimensional data: A survey on subspace cluster-
  - ing, pattern-based clustering, and correlation clustering. *ACM Transactions on Knowledge Discovery from Data (TKDD)* 3(1):1.
  - [7] Hotelling H (1933) Analysis of a complex of statistical variables into principal components. *Journal of Educational Psychology* 24(7).
  - [8] Torgerson WS (1952) Multidimensional scaling. *Psychometrika* 17(4):401–419.
  - [9] Van Der Maaten LJP, Hinton GE (2008) Visualizing high-dimensional data using t-sne. *Journal of Machine Learning Research* 9:2579–2605.
  - [10] Coifman RR, et al. (2005) Geometric diffusions as a tool for harmonic analysis and structure definition of data: diffusion maps. *Proceedings of the National Academy of Sciences of the United States of America* 102(21):7426–31.
  - [11] McInnes L, Healy J (2018) Umap: Uniform manifold approximation and projection for dimension reduction.

- arXiv preprint arXiv:1802.03426.*
- [12] Mézard M, Parisi G, Virasoro M (1987) *Spin glass theory and beyond: An Introduction to the Replica Method and Its Applications.* (World Scientific Publishing Co Inc) Vol. 9.
  - [13] Machta BB, Chachra R, Transtrum MK, Sethna JP (2013) Parameter space compression underlies emergent theories and predictive models. *Science* 342(6158):604–607.
  - [14] Transtrum MK, Qiu P (2014) Model reduction by manifold boundaries. *PRL* 113(9):1–6.
  - [15] Transtrum MK, et al. (2015) Perspective: Slowness and emergent theories in physics, biology, and beyond. *The Journal of Chemical Physics* 143(1):010901.
  - [16] Beyer K, Goldstein J, Ramakrishnan R, Shaft U (1999) When is nearest neighbor meaningful? in *International conference on database theory.* (Springer), pp. 217–235.
  - [17] Gromov M (2013) In a search for a structure, part 1: On entropy. *Preprint available at <http://www.ihes.fr/gromov>.*
  - [18] Amari S, Nagaoka H (2000) *Translations of Mathematical Monographs: Methods of Information Geometry.* (Oxford University Press) Vol. 191.
  - [19] Parisi G (1979) Infinite number of order parameters for spin-glasses. *Phys. Rev. Lett.* 43(23):1754–1756.
  - [20] Bhattacharyya A (1943) On a measure of divergence between two statistical populations defined by probability distributions. *Bulletin of the Calcutta Mathematical Society* 35.
  - [21] Abadi M, et. al. (2015) Tensorflow: Large-scale machine learning on heterogeneous distributed systems, (Google), Technical report.
  - [22] LeCun Y, Cortes C, Burges CJ (year?) Mnist database (<http://yann.lecun.com/exdb/mnist/>).
  - [23] Bishop CM (2006) *Pattern Recognition and Machine Learning.* (Springer, NY).
  - [24] Lewis A, Challinor A, Lasenby A (2000) Efficient computation of CMB anisotropies in closed FRW models. *Astrophys. J.* 538:473–476.
  - [25] collaboration P (2015) Overview of products and scientific results.
  - [26] Kullback S, Leibler RA (1951) On information and sufficiency. *Ann. Math. Statist.* 22(1):79–86.